Weierstraß-Institut

für Angewandte Analysis und Stochastik

im Forschungsverbund Berlin e. V.

Preprint ISSN 0946 – 8633

Dynamic Formation of Oriented Patches in Chondrocyte Cell Cultures

Marcus J. Grote[1], Viviana Palumberi[1], Barbara Wagner[2] Andrea Barbero [3], Ivan Martin[3]

submitted: October 31, 2010

[1] Institute of Mathematics,
University of Basel,
Rheinsprung 21,
CH-4051 Basel

[2] Weierstrass Institute for
Applied Analysis and Stochastics,
Mohrenstraße 39,
D-10117 Berlin

[3] Department of Biomedicine and Surgery,
University Hospital,
Hebelstrase 20,
CH-4031 Basel

No. 1557

Berlin 2010

2000 *Mathematics Subject Classification.* 35R09, 92C17, 35B36, 35B35.

Key words and phrases. cell alignment, pattern formation, stability, integro-partial differential equations, image processing.

Edited by
Weierstraß-Institut für Angewandte Analysis und Stochastik (WIAS)
Mohrenstraße 39
10117 Berlin
Germany

Fax: +49 30 2044975
E-Mail: preprint@wias-berlin.de
World Wide Web: http://www.wias-berlin.de/

Abstract

Growth factors have a significant impact not only on the growth dynamics but also on the phenotype of chondrocytes (Barbero et al. , J. Cell. Phys. 204, pp. 830-838, 2005). In particular, as chondrocyte populations approach confluence, the cells tend to align and form coherent patches. Starting from a mathematical model for fibroblast populations at equilibrium (Mogilner et al., Physica D 89, pp. 346-367, 1996), a dynamic continuum model with logistic growth is developed. Both linear stability analysis and numerical solutions of the time-dependent non-linear integro-partial differential equation are used to identify the key parameters that lead to pattern formation in the model. The numerical results are compared quantitatively to experimental data by extracting statistical information on orientation, density and patch size through Gabor filters.

1 Introduction

In recent years, therapies for damaged tissue have experienced great progress through the possibilities offered by new methods of tissue engineering [24]. Often these methods offer the only possibility for tissue regeneration, as in the case of cartilage, which is known to regenerate rather slowly, unlike other wound-healing processes. Most procedures pursued in tissue engineering start with a biopsy of a few cells, which are expanded *ex vivo* making use of cytokines. Those are then injected into a patient to grow tissue *in vivo*. Alternatively, scaffolds are used to provide mechanical support and structure for the tissue to be grown *in vitro* which is directly implanted. Those procedures may involve tissue replacement using donor tissue or autologous cells for *in vitro* cell-culture expansion, in order to regenerate tissue that matches the patient's native tissue.

Much research has already gone into the impact of combinations of growth factors on the proliferative capacity for a range of cell types, such as pancreatic endorcine cells, neural progenitor cells, muscle-derived stem cells [6, 7, 11, 30] and chondrocytes [3–5, 22]. For muscle-derived stem cells and chondrocyte cell cultures, mathematical models that establish characteristic kinetic parameters, such as the fraction of dividing cells and mean cell division-time have been developed [4, 11]. In addition, a logistic delay-differential model for proliferating chondrocyte cells was used to further include the effect of contact inhibition of proliferating cells upon confluence [4].

Apart from the impact of growth factors on kinetic parameters, an important focus of research concerns the effect of cytokines on the phenotype of individual cells and the

resulting organizational structure of the cell culture. Both will influence the mechanical properties of the engineered tissue, which in the case of cartilage, is intended to sustain tensile stresses and compressive loads, just as native tissue does [29]. Therefore, it is important to understand the underlying processes leading to the formation of large-scale patterns of an evolving cell culture. Identifying the relevant parameters that control these structures is the focus of the present study, combining experimental and mathematical methods [8].

In [4], human articular chondrocytes (AHAC) were isolated from cartilage biopsies and then cultured in the presence of a combination of growth factors. The individual cells assume a phenotype that closely resembles fibroblasts and eventually self-organize into regions of aligned cells, making up the monolayer of the cell culture at confluence [5]. This phenomenon has been observed before for various cell types. In principle there are a number of mechanisms that may control the formation of such patterns, ranging from chemical, adhesive or other mechanical gradients, see e.g. Trinkaus [32] for an early but instructive discussion in the context of morphogenesis.

Even in the absence of exterior influences, however, Elsdale [14] discovered that proliferating fetal lung fibroblasts form parallel arrays during *in vitro* cell expansion. Similar results were found for BHK fibroblasts in the experimental study by Erickson [15]. In [14] Elsdale argued that the intrinsic property of fibroblasts is to move unless prevented to do so by the environment and hence that patterns form solely due to direct cell-cell interactions to enable maximal motility. Under the assumption of contact inhibition Erickson[15] concluded from a series of cell-cell contact experiments, that if the lamellipodium of a cell in ruffling mode contacts another cell at a certain angle, the direction of motion changes depending on that part of the leading edge of the lamellipodium which made contact and where ruffling is stopped. This mechanism is employed by Erickson to explain the existence of a critical angle above which cells cease to align. This critical angle seems to differ for different cell types, e.g. about 20^o for fetal lung fibroblasts and approximately 50^o for BHK cells. For fibroblasts the leading edge of the lamellipodium is much narrower than for the BHK fibroblasts. Hence, except for rather narrow contact events, motion will halt (else cells may even criss-cross other cells). Moreover, similar behavior is observed for contact events of already established arrays of aligned cells. This behavior is eventually reflected in the resulting patterns at confluence.

Mathematical modeling of the dynamical process of array formation of aligned cells started with the work by Edelstein-Keshet and Ermentrout [13]. The continuum models derived for pattern forming cell cultures assume random spatial and orientational distributions of the cells that are attracted (repulsed) and change their direction of motion as response to cell-cell interactions. Here define the cell density depends on time, two-dimensional physical space and the angle of orientation. The range of interaction is kept small in order to model the local character cellular interactions. Apart from terms modeling the random motion in physical and angular space, the model includes a term that describes the probability of alignment of cells as a response to cell-cell contact, which vanishes outside the range of angles known to lead to align-

ment. In subsequent articles the resulting system of integro-differential equations for free cells and cells already bound to an array are discussed in various limiting cases and analysed with respect to their stability about the homogeneous state [26]. Similar models were also used for other pattern forming processes such as swarming or the dynamics of actin binding fibers [9, 26, 28].

Here we extend these models to include time-dependent logistic growth to account for the later stages of *in vitro* chondrocyte cell expansions. In fact, one important aspect of our study is to enable a direct comparison with our experimental results in section 2.1. The analysis of the experimental results and, in particular, the classification of the cells within angular space is realized by using two-dimensional Gabor filters [10] for the experimental images and is described in section 2.3. In section 3, we present our mathematical model, followed by analysis and the description of our numerical algorithm to solve the time-dependent nonlinear integro-partial differential equation in section 4. In section 5 we investigate the stability of the solution via a linear stability analysis about the homogeneous state and compare those findings to the results of the full nonlinear model. Finally, quantitative comparisons with experimental data are performed in section 6.

2 Biological background

2.1 The impact of growth factors

Depending on the cell type and the specific growth factors used, cytokine-induced proliferation of cells can generally be characterized by one or more parameters, such as a shorter cell division time, a shorter time until first cell division, or lower percentage of remaining quiescent cells [4, 11, 12]. Those key parameters can be obtained, for instance, by combining a logistic delay-differential model with the results from specific micro-colony experiments [4]. From that model, Barbero et al. established in the case of adult human articular chondrocytes(AHAC) expansion in a medium with added growth factors TFP that the time of first cell division is about 1.4 times shorter and the percentage of quiescent cells about 1.7 times smaller than in the absence of TFP.

Further characteristics observed in experiments [4] concern the elongated shape the cells assume when cultured in a medium with TFP. During the sigmoidal growth of the cell culture, individual cells are initially oriented at random. As the population approaches confluence, cells tend to locally align and form coherent structures. Those spatial patterns appear highly irregular while individual patches greatly vary both in shape and size, without clear boundaries between them – see Fig. 1.

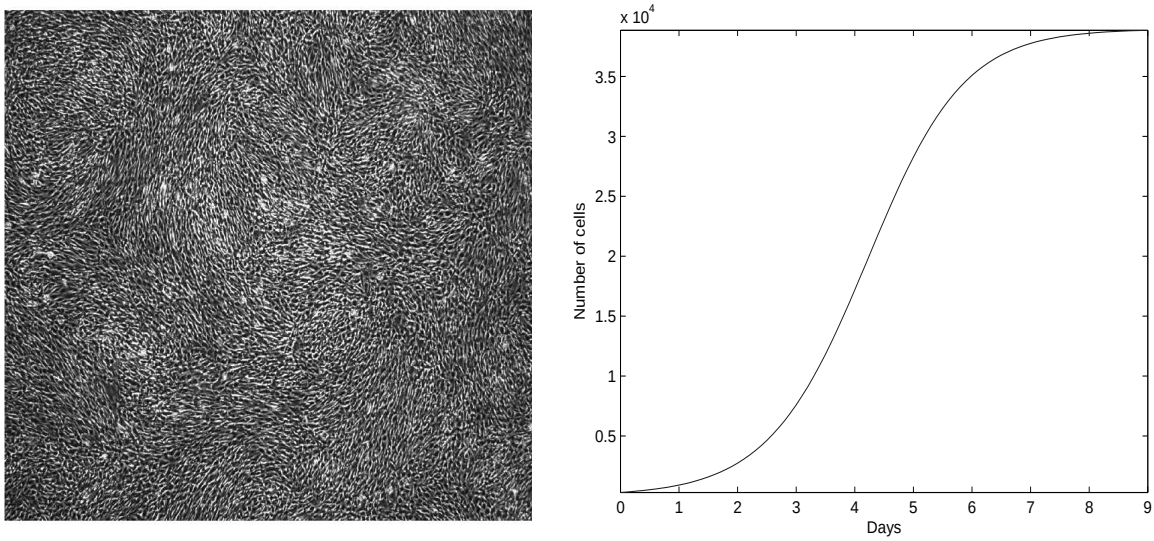

Figure 1: *Original image of AHAC cells cultured with TFP at day 9 near confluence (left). Sigmoidal evolution of number of cells vs. time (right)*

2.2 Cell culture: isolation and expansion

To monitor patch formation and obtain quantitative experimental data on diffusion constants, we track the motion of an ensemble of individual AHAC cells up to confluence. Here full-thickness human articular cartilage samples were collected from the femoral lateral condoyle of two individuals (patient A: male, 18 years old, patient B: male, 66 years old), with no history and no radiographic signs of joint disease, after informed consent and in accordance with the local Ethical Commission. Human adult articular chondrocytes (AHAC) were isolated using 0.15% type II collagenase for 22 hours and cultured for one passage in Dulbeccos modified Eagles medium (DMEM) containing 10% foetal bovine serum, 4.5 mg/ml D-Glucose, 0.1 mM nonessential amino acids, 1 mM sodium pyruvate, 100 mM HEPES buffer, 100 U/ml penicillin, 100 ţg/ml streptomycin, and 0.29 mg/ml L-glutamine and supplemented with the 1 ng/ml of Transforming Growth Factor-b1 (TGF-b1), 5 ng/ml of Fibroblast Growth Factor-2 (FGF-2) and 10 ng/ml of Platelet-Derived Growth Factor-BB (PDGF-BB) (growth factor medium, TFP) in a humidified 37^{o}C/5% CO2 incubator as previously described [4]. When cells were approximately 80% confluent, first passage (P1) cells were rinsed with phosphate buffered saline, detached using 0.05% trypsin/0.53mM EDTA and frozen in complete medium containing 10% dimethylsulfoxid. AHAC after thawing were then used for the studies described below.

Monitoring of cell expansion until confluence AHAC were re-plated in two wells of a 6 well plate at a density of 10000 cells/cm^2 and cultured in growth factor medium up to 10 days in a humidified 37^{o}C/5% CO2 incubator with daily culture medium change. AHAC cultures were monitored by phase contrast microscopy and pictures

were taken from random areas of the wells each day.

Study of cell movement AHAC were re-plated in a 6 well plate at different densities, which were 200, 3000, 10000, 15000 and 20000 cells/cm^2, and cultured in growth factor medium for 1 day in a humidified 37^{o}C/5% CO2 incubator. Next, the plate was transferred to the incubator of the Olympus system. From a time-lapse microscope we obtained a sequence of frames which we used to monitor cell motion. Snapshots were taken at 15 minute intervals, which corresponds to an average travel distance of $9\mu m$, to provide sufficient space-time resolution compared to the typical length of a cell ($50\mu m$). With the software analySIS^D we performed a manual tracking in all five wells (Fig. 2) to follow about 100 cells for each density, for 12 hours, a duration that allowed us to neglect cell doubling.

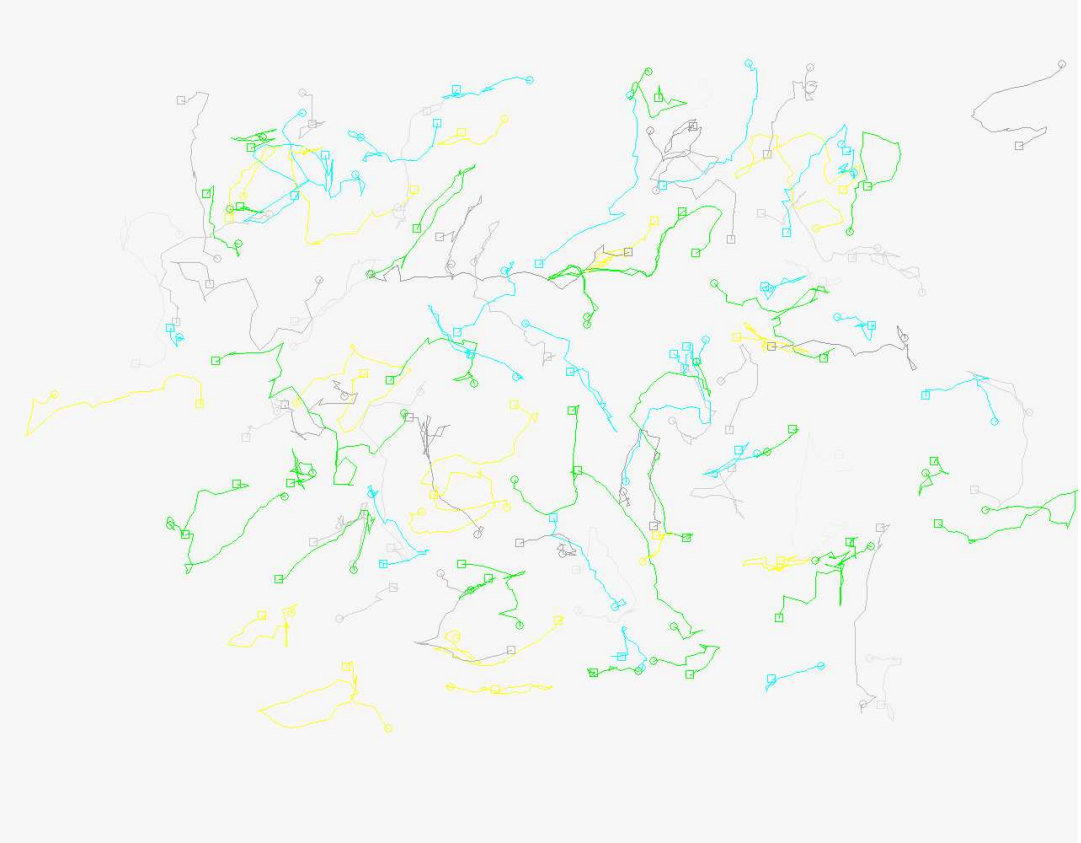

Figure 2: *Tracking of individual cells at density 20000/cm^2.*

Spatial diffusion To estimate the spatial diffusion, we performed experiments at various densities (i.e. 200, 3000, 10000, 15000, 20000 cells/scm) and for each density we manually tracked individual cells in three different areas of the well. Assuming Brownian motion, the diffusion coefficient D is related to the mean square displacement, $< X^2 >$, through the relation $< X^2 >= 2Dt$. A linear least-squares fit of the

time evolution of the mean square distance then yields D. From those estimates at varying density, shown in table 1, we obtained the constant average diffusion coefficient $D = 0.29\,\mu m^2/s$.

cells/scm	200	3000	10000	15000	20000
coeff D1	0.31	0.30	0.37	0.31	0.31
coeff D2	0.18	0.23	0.32	0.30	0.26
coeff D3	0.23		0.40	0.34	0.30
mean $\pm$ SD	0.24 ± 0.07	0.26 ± 0.04	0.36 ± 0.04	0.31 ± 0.02	0.30 ± 0.03

Table 1: Estimates of the diffusion constant D at three different locations inside the well and at varying density, together with the mean values $\pm$ SD.

2.3 Image analysis of alignment

Standard image segmentation algorithms proved unable to distinguish between individual cells and the background. Thus to identify patches of alignment and estimate their size quantitatively, both in the numerical simulations and in the experiment, we proceed in two steps. First, we apply a special class of filters to images such as Fig. 1 that reveal the dominant local axis of orientation. Second, we estimate the average size of cell clusters with a common orientation with a discrete statistical measure, which is then used to compare numerical simulations with experiments.

To classify cells according to their orientation, we opt for Gabor filters [17, 19] which consist of a local Gaussian kernel of width σ, multiplied by a plane wave with distinct orientation θ and frequency ω:

$$G(x', y') = \exp\left\{-\frac{1}{2}\left(\left(\frac{x'}{\sigma}\right)^2 + \left(\frac{y'}{\sigma}\right)^2\right)\right\}\cos(2\pi\omega x')$$
$$x' = x\,\cos(\theta) + y\,\sin(\theta), \quad y' = y\cos(\theta) - x\sin(\theta),$$

where unit length in x (or y) corresponds to a single pixel. The typical width $\sigma = 12$ and frequency $\omega = 0.08$ for an array of aligned cells were determined a priori and remained fixed in all further analysis – see Fig. 3. Hence Gabor filters locally respond to patterns with spatial frequency ω and orientation θ, within a subregion of size σ. Their two-dimensional extension is commonly used in image analysis and computer vision; they were also proposed as a model for the spatial summation properties of simple cells in the visual cortex [10].

To any image we apply a suite of Gabor filters for varying orientation at 45° intervals and assign to each pixel location (i, j) a distinct color c_{ij} that corresponds to the highest filter response. Hence c_{ij} reflects the dominant orientation at location (i, j), and cells aligned with that particular orientation are thus revealed, as shown in Fig. 4.

Next, we estimate the typical cluster in a filtered image, such as in Fig. 4, either from epxeriment or numerical simulation. To do so, we assign to each pixel (i, j) the value

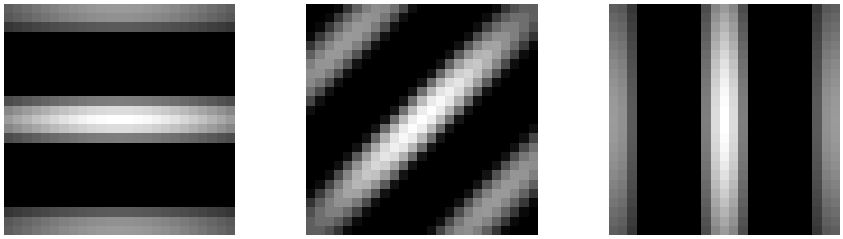

Figure 3: *Gabor filters with frequency* $\omega = 0.08$*, scale* $\sigma = 12$*, and orientations* $\theta = 0, \pi/4, \pi$*.*

$p_{ij}(s) = 1$ if it belongs to a cluster of size s, that is if at least 50% of the points within distance s are of the same color; else, we set $p_{ij}(s)$ to zero. Summation over all pixels yields an estimate $r(s)$ of the number of pixels belonging to a cluster of size s as

$$r(s) = \sum_{ij} p_{ij}(s), \quad p_{ij}(s) = \begin{cases} 1 \\ 0 \end{cases} . \tag{2.1}$$

The intersection of $r(s)$ with the s-axis yields a reliable estimate for the typical patch size, i.e. the largest cluster size, as illustrated with synthetic black and white data in Fig. 5. Moreover, comparison of the left and right frames in Fig. 5 demonstrates that the intersection of $r(s)$ with the s-axis is rather insensitive to added random noise.

3 Mathematical Model

3.1 Formulation

Starting form the pioneering works of Edelstein-Keshet et al. [13, 26, 27], we now build a continuum model to describe the time evolution of a cell population of density $C(\theta, \vec{x}, t)$ in angle θ and two-dimensional space $\vec{x} = (x, y)$ at time t. During initial times the cells are essentially free to move in space and also turn their axis of orientation at random, similarly to fibroblasts. As the population density increases, however, cells come into contact. In [13–15] the underlying mechanism responsible for the directional motion and the resulting pattern formation is explained solely on the basis of single cell contact events for the case of related fibroblast cell cultures. This mechanism is a form of contact inhibition that cells experience when their lamellipodium touch. Indeed whenever mutual contact occurs within a small angle and hence only a portion of the lamellipodium touches, the cells alter their orientation accordingly and align, as observed by Elsdale [14].

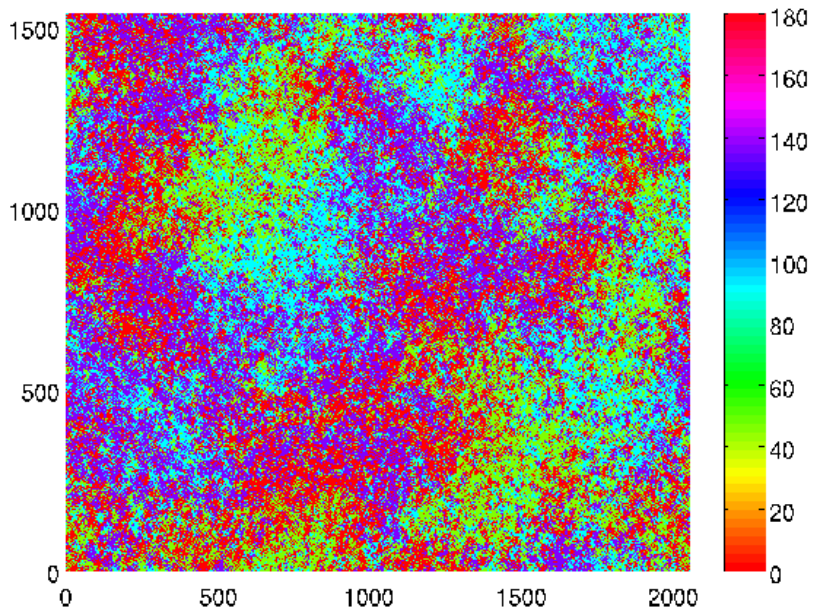

Figure 4: *The effect of Gabor filtering applied to Fig. 1. The color indicates the dominant local direction of alignment.*

Following [27] we now let $W(\vec{x}-\vec{x}',\theta,\theta')$ denote the rate at which a cell at $\vec{x}'$ and θ' moves to $\vec{x}$ and rotates to θ due to the impact of any surrounding cells. The angular velocity associated with this motion is then given by the gradient of W at angle θ and position $\vec{x}$, due to the cumulative interaction with all other cells:

$$\frac{\partial}{\partial\theta}(W\star C)(\vec{x},\theta,t) := \frac{\partial}{\partial\theta}\int W(\vec{x}-\vec{x}',\theta,\theta')C(\theta',\vec{x}',t)\,d\theta' d\vec{x}'. \tag{3.1}$$

The gradient of the associated flux $C\,\partial_\theta(W\star C)$ then induces convective motion towards locations of higher concentration which corresponds to aggregation in space and alignment in angle; both compete with the inherent tendency of cells for random motion modelled by diffusive terms.

Following [27] we assume that the probabilities to align or to aggregate are independent of each other, hence

$$W(\vec{x}-\vec{x'},\theta,\theta') = W_1(\theta-\theta')W_2(\vec{x}-\vec{x'}). \tag{3.2}$$

Experiments suggest that the probability of alignment W_1 decreases as the relative angle between neighboring cells increases [14], whereas beyond a critical angle α cells no longer align; hence, W_1 is positive and non-increasing for $0\le\theta\le\alpha$ but vanishes for $\alpha<\theta\le\pi$. Since clockwise and anticlockwise turns are equally probable, W_1 must also be even. For simplicity, we assume that W_1 is Gaussian with mean zero and standard deviation σ, and set $\alpha=2\sigma$; other choices are possible and discussed

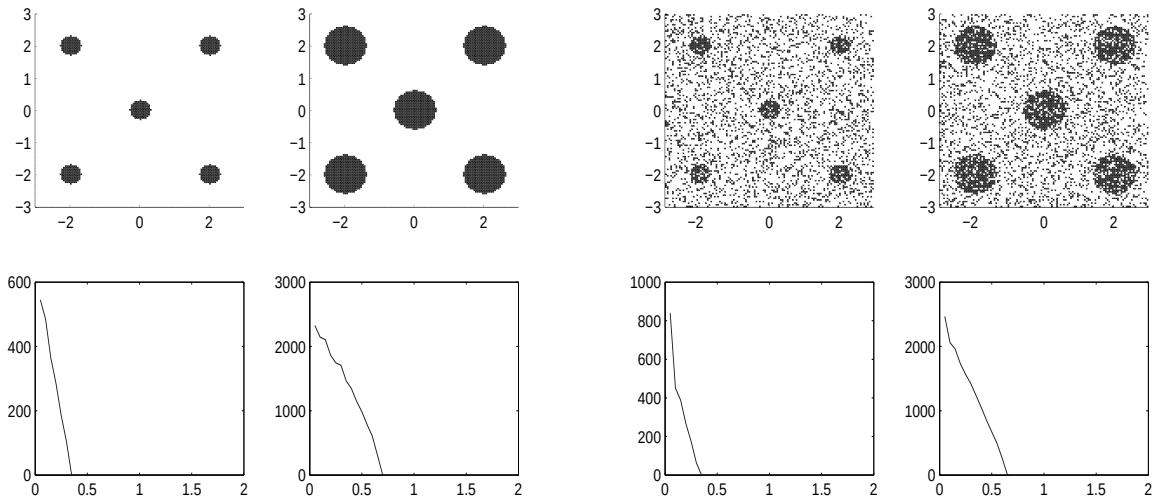

Figure 5: *Estimate of cluster size from synthetic texture images (top left) and corresponding cluster size function $r(s)$, as in (2.1) (bottom left). The intersection of $r(s)$ with the s-axis yields a robust estimate of the cluster size, even in the presence of added random noise (right).*

in [13]. After normalization, we thus obtain

$$W_1(\theta) = \frac{1}{\alpha\sqrt{2\pi}} e^{-\frac{2\theta^2}{\alpha^2}}, \quad |\theta| < \alpha. \tag{3.3}$$

Since the strength of cell-to-cell interactions decreases with growing distance [13], we again choose a Gaussian kernel for W_2,

$$W_2(\vec{x}) = \frac{1}{2\sigma^2\pi} e^{-\frac{|\vec{x}|^2}{2\sigma^2}}, \quad \vec{x} \in [-L_x, L_x] \times [-L_y, L_y], \tag{3.4}$$

where L_x and L_y denotes the size of the domain.

Our previous experiments indicate that the growth rate slows down, as the cell density increases locally in space, and that it eventually vanishes when the carrying capacity is reached because of limited space. Therefore we model cell growth by a logistic term with growth rate ρ, where the growth rate reduction is determined by the population density at x and t, that is by the marginal probability density $\int_{-\pi}^{\pi} C(t, x, y, \theta) d\theta$. This leads to the full model equations:

$$\begin{aligned} \frac{\partial C}{\partial t} &= \epsilon_1 \frac{\partial^2 C}{\partial \theta^2} + \epsilon_2 \left(\frac{\partial^2 C}{\partial x^2} + \frac{\partial^2 C}{\partial y^2} \right) \\ &\quad -\gamma \frac{\partial}{\partial \theta} \left(C \left[\frac{\partial W}{\partial \theta} * C \right] \right) - \gamma \left\{ \frac{\partial}{\partial x} \left(C \left[\frac{\partial W}{\partial x} * C \right] \right) + \frac{\partial}{\partial y} \left(C \left[\frac{\partial W}{\partial y} * C \right] \right) \right\} \\ &\quad +\rho\, C \left(1 - \frac{L_x\, L_y}{K} \int_{-\pi}^{\pi} C(t, x, \theta) d\theta \right). \end{aligned} \tag{3.5}$$

Here ϵ_1 and ϵ_2 denote diffusion coefficients, while γ denotes a drift coefficient.

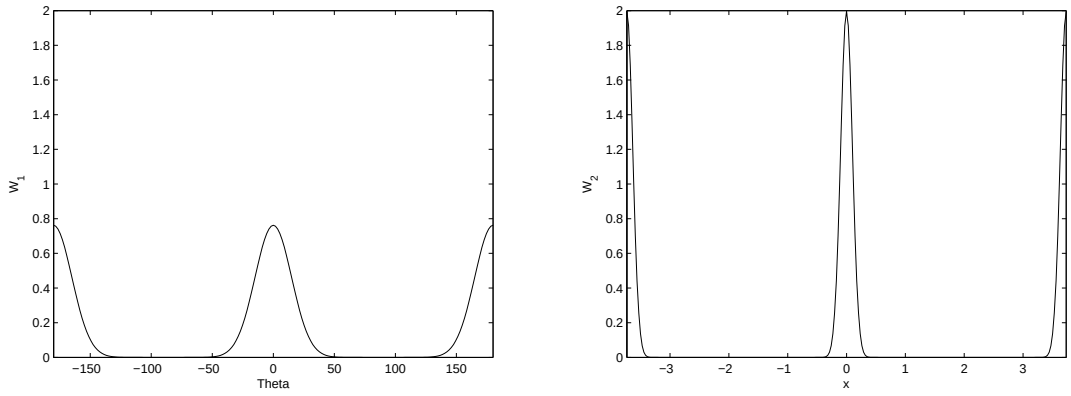

Figure 6: *The kernels W_1 and W_2 from (3.3) and (3.4): W_1 (left) and W_2 (right).*

3.2 Existence of weak solutions

We now show existence of a weak solution of (3.5) until time $T > 0$ in $U_T = U \times (0, T]$, where $U = (-\pi, \pi) \times D$, $D = (0, L_x) \times (0, L_y)$. First we nondimensionalize the governing equations as follows, with

$$C^* = \frac{C}{K} L_x L_y, \quad t^* = \rho t, \quad \theta^* = \theta \sqrt{\frac{\rho}{\epsilon_1}}, \quad x^* = x \sqrt{\frac{\rho}{\epsilon_2}}, \quad y^* = y \sqrt{\frac{\rho}{\epsilon_2}}$$

and

$$\alpha^* = \alpha \sqrt{\frac{\rho}{\epsilon_1}}, \quad \sigma^* = \sigma \sqrt{\frac{\rho}{\epsilon_2}}.$$

Dividing by $K\rho/(L_x L_y)$ and dropping the '$*$' for simplicity of notation, we thus obtain the nondimensional form of (3.5):

$$\begin{cases} \partial_t C &= \text{div}(\nabla C) - A\,\text{div}(C \nabla W * C) + f(C) & \text{in } U_T \\ C &= g & \text{on } U \times \{t = 0\}, \end{cases} . \tag{3.6}$$

with initial condition $g : U \to \mathbb{R}$, $f(C) = C\left(1 - \int_{-\pi}^{\pi} C d\theta\right)$, and $A = K\gamma/(L_x L_y \epsilon)$; without loss of generality we assume $\epsilon_1 = \epsilon_2 = \epsilon$ here.

Next, we multiply (3.6) by a test function $v \in H^1_{per}(U)$ and integrate by parts to obtain the weak form

$$< C', v > + (\nabla C, \nabla v) = A\,(C \nabla W * C, \nabla v) + (f(C), v) \tag{3.7}$$

for each $v \in H^1_{per}(U)$, $0 < t \leq T$ and $C(0) = g$. Here $<, >$ denotes the standard dual pairing between $H^{-1}(U)$ and $H^1_{per}(U)$, the Sobolev space of H^1 periodic functions, and C now corresponds to a mapping $C : [0, T] \to H^1_{per}(U)$ – see [16] for further details. Thus to show existence of a weak solution for (3.6) means that we must show existence of a function

$$C \in H^1(0, T; H^1_{per}(U)), \quad \text{with } C' \in L^2(0, T; H^{-1}(U)),$$

which solves (3.7). The proof is based on a Galerkin projection of $C(t)$ on a finite dimensional subspace and requires various estimates and technical results summarized in the three lemmas below; their proofs are listed in the appendix.

Lemma 3.1. (Boundedness) *Let C be a smooth and bounded solution of equation (3.6). If $C(0) \geq 0$ in U, then $C(t) \geq 0$, $\forall 0 \leq t \leq T$, and the mass remains bounded, i.e.*

$$\|C(t)\|_{L^1(U)} \leq K_1 := e^T \|C(0)\|_{L^1(U)}. \tag{3.8}$$

Next we let $\{w_k\}_{k=1}^{\infty}$ denote an orthogonal basis of smooth basis functions of $H^1_{per}(U)$, which also form an orthonormal basis of $L^2(U)$. For the Galerkin projection $C_m(t)$ of $C(t)$ we then have the following result.

Lemma 3.2. (Galerkin construction) *For each integer $m = 1, 2, \ldots$ there exists a unique function $C_m : [0, T] \to H^1_{per}(U)$ of the form*

$$C_m(t) := \sum_{l=1}^{m} d_m^l(t) w_l, \tag{3.9}$$

with

$$d_m^l(0) = (g, w_l), \quad l = 1, \ldots, m, \tag{3.10}$$

which solves the problem

$$(C_m', w_k) + (\nabla C_m, \nabla w_k) = A\,(C_m \nabla W * C_m, \nabla w_k) + \int_U f(C_m)\, w_k \tag{3.11}$$

for $0 \leq t \leq T$, $k = 1, \ldots, m$.

For simplicity, we now assume that the functions C_m are nonnegative with bounded mass.

Lemma 3.3. (Energy estimate) *If the functions C_m defined in (3.9) are nonnegative and have a bounded mass, there exists a constant K that depends only on U, T, such that*

$$\max_{0 \leq t \leq T} \|C_m(t)\|_{L^2(U)} + \|C_m\|_{L^2(0,T;H^1_{per}(U))} + \|C_m'\|_{L^2(0,T;H^{-1}(U))} \leq K \|g\|_{L^2(U)}. \tag{3.12}$$

Passing to the limit $m \to \infty$ in the Galerkin procedure, we thus find a weak solution of (3.6), as shown below.

Theorem 3.4. *If the functions C_m, defined in (3.9), are nonnegative and have bounded mass, there exists a weak solution of (3.6).*

Proof. According to the energy estimates (3.12), we see that the sequence $\{C_m\}_{m=1}^{\infty}$ is bounded in $L^2(0, T; H^1_{per}(U))$ and $\{C_m'\}_{m=1}^{\infty}$ is bounded in

$L^2(0,T;H^{-1}(U))$. Consequently there exists a subsequence $\{C_{m_l}\}_{m_l=1}^{\infty} \subset \{C_m\}_{m=1}^{\infty}$ and a function $C \in H^1(0,T;H^1_{per}(U))$, with $C' \in L^2(0,T;H^{-1}(U))$, such that

$$\begin{aligned} C_{m_l} &\rightharpoonup C \quad \text{in} \in L^2(0,T;H^1_{per}(U)) \\ C'_{m_l} &\rightharpoonup C' \quad \text{in} \in L^2(0,T;H^1_{per}(U)). \end{aligned} \tag{3.13}$$

Next, we fix an integer N and choose a function $v \in C^1([0,T];H^1_{per}(U))$ of the form

$$v(t) = \sum_{k=1}^{N} d^k(t) w_k, \tag{3.14}$$

where $\{d^k\}_{k=1}^N$ are given smooth functions. We choose $m \geq N$, multiply (3.11) by $d^k(t)$, sum over $k = 1, \ldots, N$ and integrate in time to obtain

$$\int_0^T \left[< C'_m, v > + (\nabla C_m, \nabla v) \right] dt = A \int_0^T (\nabla v, C_m \nabla W * C_m)\, dt + \int_{U_T} f(C_m)\, v. \tag{3.15}$$

Then we set $m = m_l$ and recall (3.13), which yields in the weak limit

$$\int_0^T \left[< C', v > + (\nabla C, \nabla v) \right] dt = A \int_0^T (\nabla v, C \nabla W * C)\, dt + \int_{U_T} f(C)\, v. \tag{3.16}$$

By density (3.16) holds for all $v \in L^2(0,T;H^1_{per}(U))$ and therefore we have

$$< C', v > + (\nabla C, \nabla v) = A\,(\nabla v, C \nabla W * C) + \int_U f(C)\, v \tag{3.17}$$

for each $v \in H^1_{per}(U)$ a.e. $0 \leq t \leq T$. Furthermore $C \in C([0,T];L^2(U))$ and therefore $C(0) = g$ – see [16] for details. □

4 Numerical Methods

We restrict the computations to a small subregion Ω inside the experimental well. Thus, boundary effects due to the finite size of the well are negligible and we may impose periodic boundary conditions at the boundary of the computational domain $\Omega = [0, L_x] \times [0, L_y]$. For the numerical approximation of (3.5) all spatial derivatives are approximated by second-order centered finite differences on a regular grid. The convolution integrals are computed by trapezoidal quadrature, which yields exponential convergence for periodic analytic functions [23]. Hence the numerical discretization error is second-order accurate in space and angle.

For parabolic problems standard explicit Runge-Kutta schemes impose rather stringent restrictions on the time-step for numerical stability, typically $\Delta t \leq C \Delta x^2$, and hence are notoriously inefficient [21]. In contrast, implicit methods waive those time-step restrictions but would require here the solution of a nonlinear integro-differential boundary value problem at every time step, a rather high price to pay.

To avoid the above mentioned difficulties, we opt for Runge-Kutta-Chebyshev methods instead, which are fully explicit while allowing larger time-steps. Instead of maximizing the accuracy, RK-Chebyshev methods maximize the interval $[-\ell, 0]$ of the negative real axis contained in the stability region [21, 25]. Because ℓ is proportional to s^2, for a fixed number of stages, s, any reduction of the mesh size Δx can be counterbalanced by an equivalent increase of the number of stages while keeping the time-step Δt fixed. Therefore RK-Chebyshev methods circumvent the crippling quadratic increase in the number of time-steps of traditional RK methods that results from any linear reduction of the mesh size [2, 18, 33].

For instance, the first-order s-stage RK-Chebyshev method for the initial-value problem

$$y'(t) = f(y), \qquad y(0) = y_0, \tag{4.1}$$

is given by

$$g_0 = y_0, \tag{4.2}$$
$$g_1 = y_0 + (1/s^2)\Delta t f(g_0), \tag{4.3}$$
$$g_i = (2/s^2)\Delta t f(g_{i-1}) + 2g_{i-1} - g_{i-2}, \tag{4.4}$$
$$y_1 = g_s. \tag{4.5}$$

In Figure 7 we observe that the stability regions of the 3-stage RK-Chebyshev method is about nine times larger than that of the standard fourth-order RK4. Following [20], we eliminate the two intersections where the stability region shrinks to zero by adding small damping of size $\epsilon > 0$. Let $\epsilon > 0$ and $T_s(x)$ denote the Chebyshev polynomial of degree s [1]. Then the damped RK-Chebyshev method for (4.1) is given by

$$g_0 = y_0, \tag{4.6}$$
$$g_1 = y_0 + \Delta t(w_1/w_0) f(g_0), \tag{4.7}$$
$$g_i = \frac{1}{T_i(w_0)}\left[2w_1\Delta t T_{i-1}(w_0) f(g_{i-1}) + 2w_0 T_{i-1}(w_0) g_{i-1} - T_{i-2}(w_0) g_{i-2}\right], \tag{4.8}$$
$$y_1 = g_s. \tag{4.9}$$

where

$$R_s(z) = \frac{1}{T_s(w_0)} T_s(w_0 + w_1 z), \quad w_0 = 1 + \frac{\epsilon}{s^2}, \quad w_1 = \frac{T_s(w_0)}{T_s'(w_0)}. \tag{4.10}$$

As illustrated in Fig. 7 for $\epsilon = 0.05$, the stability domain is now slightly shorter (by a factor $4\epsilon s^2/3$), but its boundary remains at a safe distance form the real axis [20].

When the right-hand side in (4.1) explicitly depends on time, the terms involving $f(g_i)$ in (4.6)–(4.9) are replaced by $f(g_i, t_i)$. The precise times $t_i \in [0, \Delta t]$ where f needs to be evaluated are determined by augmenting (4.1) with the trivial differential equation,

$$z'(t) = 1, \qquad z(0) = t_0 \tag{4.11}$$

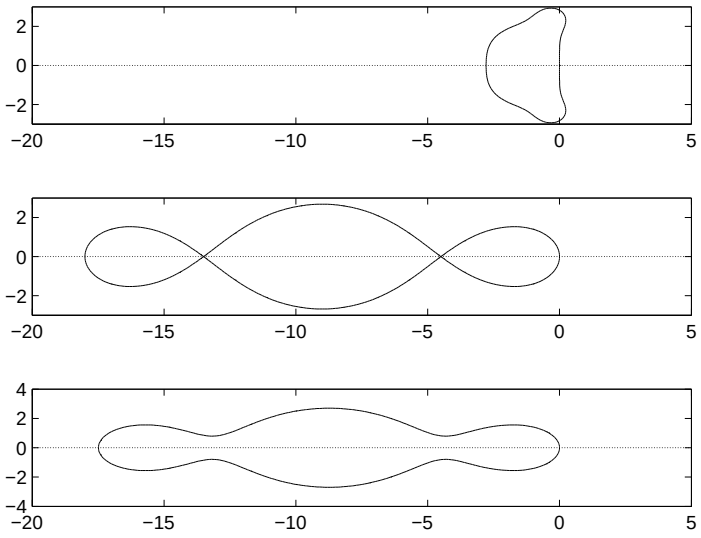

Figure 7: *Stability regions: fourth-order RK4 (top) and first-order 3-stage Chebyshev methods without damping (middle) and with damping (bottom). The stability regions of the RK-Chebyshev method is about nine times larger then that of the standard RK4.*

and applying (4.6)–(4.9) to it. Thus for $t \in [0, \Delta t]$ we have

$$t_0 = 0, \tag{4.12}$$

$$t_1 = \Delta t(w_1/w_0), \tag{4.13}$$

$$t_i = \frac{1}{T_i(w_0)}\left[2w_1\Delta t T_{i-1}(w_0)) + 2w_0 T_{i-1}(w_0)t_{i-1} - T_{i-2}(w_0)t_{i-2}\right], \tag{4.14}$$

and so forth during subsequent time steps.

5 Stability

Linear stability analysis Before investigating numerically the emergence of coherent patterns in the full nonlinear model (3.5), it is instructive to investigate the stability properties of the homogeneous state, i.e. the state, where the density of cells in angular and spatial space is distributed evenly. Linear stability analysis characterizes the effect of small perturbations on the early time evolution in angular and spatial space. We therefore expect good agreement with the early stages of the numerical solution of the fully nonlinear model (3.5).

If $\rho = 0$, the homogeneous state $C \equiv \bar{C}$ is an exact solution of (3.5), since we then have $W \star C = C$. In this case, linearization of (3.5) about $C \equiv \bar{C}$ using the ansatz

$$C(\vec{x}, \theta, t) = \overline{C} + \delta\, C'_{n,q}(\vec{x}, \theta, t), \tag{5.1}$$

where the amplitude of the perturbation $\delta \ll 1$ is small, results in an eigenvalue problem for the integro-differential operator previously analyzed in [13, 27]. In particular, Mogilner et al. [27] showed for an unbounded spatial domain that the functions

$$u_{q_1}(x) = e^{iq_1 x}, \;\; u_{q_2}(y) = e^{iq_2 y}, \;\; z_n(\theta) = e^{in\theta}, \qquad q_1, q_2 \in \mathbb{R} \tag{5.2}$$

form a complete set of orthogonal eigenfunctions for the spatial and angular Laplace operator with eigenvalues q_1, q_2 for the spatial and $n = 0, 1, 2, ...$ for the angular diffusion operator, respectively. In addition, they proved that (5.2) are not only the eigenfunctions of the Laplace operators, but also of the convolution operators W_1* and W_2*, where the eigenvalues are the Fourier coefficients denoted by $\hat{W}_n$ and $\hat{W}_q = \hat{W_{q_1}} \hat{W_{q_2}}$, where $q = \sqrt{q_1^2 + q_2^2})$ and

$$\hat{W}_n = \frac{1}{\pi} \int_{-\pi}^{\pi} W_1(\theta) e^{-in\theta} d\theta, \qquad \hat{W}_{q_j} = \int_0^{L_{x_j}} W_2(x_j) e^{-iq_j x_j} dx_j \,, \tag{5.3}$$

where $j = 1, 2$ and $x_1 = x, x_2 = y$. From the normal modes ansatz

$$C'_{n,q}(\vec{x}, \theta, t) = e^{\lambda t} \, u_{q_1}(x) \, u_{q_2}(y) \, z_n(\theta) \tag{5.4}$$

the stability of the homogeneous state is then found from the solution of the equation

$$\lambda = -r + \overline{C} \, s \,, \tag{5.5}$$

where

$$r = (\epsilon_1 n^2 + \epsilon_2 q^2) \quad \text{and} \quad s = \hat{W}_q \hat{W}_n \gamma (n^2 + q^2) \tag{5.6}$$

for all q_1, q_2 and n. Hence the condition for instability of the homogeneous solution is given by $\lambda > 0$. Thus, any increase in the diffusion coefficients ϵ_1, ϵ_2 tends to stabilize the system, while the cell-to-cell interaction terms $\hat{W}_n$ and $\hat{W}_q$ tend to destabilize the system, for increasing values of n, q, unless W_n is zero. Moreover, for any particular values of $\epsilon_1, \epsilon_2, n, q$, the constant state $\bar{C}$ becomes unstable at sufficiently high cell density, unless $\hat{W}_n$ or $\hat{W}_q$ vanishes.

For our extended model with logistic growth, where $\rho \neq 0$, the homogeneous state about which we linearize is now time-dependent, due to the slow mass increase. Thus we make the ansatz

$$C(\theta, \vec{x}, t) = \overline{C}(t) + \delta \, C'_{n,q}(\theta, \vec{x}, t) \tag{5.7}$$

with $C'_{n,q} = \hat{C}_{n,q}(t) e^{i(qx + n\theta)}$, since now the standard normal modes ansatz may lead to non-normal linear systems with non-orthogonal eigenfunctions – see [31], for instance, for a more detailed discussion of such problems in the context of hydrodynamics. Our slightly more general ansatz for $C(\theta, \vec{x}, t)$ then leads to the following differential equation for $\hat{C}_{n,q}$

$$\frac{d\hat{C}_{n,q}}{dt} = \left[-(\epsilon_1 n^2 + \epsilon_2 q^2) + \overline{C}(t) \, \hat{W}_q \hat{W}_n \gamma (n^2 + q^2) + \rho \left(1 - \frac{\overline{C}(t)}{\kappa} \right) \right] \hat{C}_{n,q}(t) \,, \tag{5.8}$$

where

$$\overline{C}(t) = \frac{\kappa}{1 + C_1 \kappa e^{-\rho t}} \tag{5.9}$$

is the solution of the leading order problem and represents the slowly growing mass until the carring capacity is reached. The constant $C_1 = 1/\overline{C}(0) - 1/\kappa$, where $\overline{C}(0)$ is chosen to be the same as $\bar{C}$ in the original problem and we denote $\kappa = K/(2\pi L_x L_y)$. Hence, the growth rate is given here by

$$\ln(\hat{C}_{n,q}(t)) = (-r + s\kappa)t + \frac{s\,\kappa - \rho}{\rho} \ln\left(1 + C_1 \kappa\, e^{-\rho t}\right) + const. \tag{5.10}$$

We note that now the additional parameter K, the carrying capacity, will have a decisive impact on the stability properties of the solutions.

Comparison of the full model with linear stability To compare the results from linear stability analysis to those from the numerical simulation of the full problem, we choose as an example the simple case for which $\rho = 0$ and $\gamma = 1$. We take the (constant) base state $\bar{C} = 25$, let $\epsilon_1 = 0.0025$ and $\epsilon_2 = 0.5$ so that for $n > 0$ and $q = 0$ the base state is unstable according to linear stability analysis. Now, we determine n_{max} such that the growth rate is maximal, i.e. $\sigma_{max} = \sigma(n_{max}, q_{max})$ (here $q = q_{max} = 0$). Thus, we can find n_{max} which is at most $O(1)$ with a σ_{max} not too small, together with the the corresponding eigenfunction $C'_{n,q}$ and a corresponding asymptotic growth rate λ .

Next, we initialize our nonlinear simulation with the initial data

$$\bar{C} + \delta C'_{n,q}\,, \quad \text{such that} \quad \delta \leq \min\left(0.1,\ 0.1\,\frac{\sigma_{max}}{n_{max}^2}\right)$$

to ensure that the correction term does not invalidate the original assumptions of linear stability analysis.

In figure 8 we plot $\log ||C||$,

$$||C|| := \frac{\max_{\theta,x,y}|C(\theta,x,y,t) - \bar{C}|}{\delta} \quad \text{versus} \quad t\,,$$

both for the solution of the fully nonlinear model and for that from linear stability. Note that the growth rate of the linearized problem for the extended model, i.e. where $\rho \neq 0$, now also depends on time. Once initial transients have died out, both models agree, as expected. As time progresses, however, the dynamics of the full model deviate from those of the linearized problem. Thus, the evolving patterns may deviate from those predicted by linear stability theory, in particular, at later times as the cell culture reaches confluence, depending on parameter values.

In figure 8 we show a comparison of the growth rates for the fully nonlinear and the linearized models, for the set of paramters given at the beginning of this paragraph. This example illustrates that generically the following behaviour is established. For the case of $\rho = 0$ we observe agreement right from the beginning, since we perturbed with the exact eigenfunctions as in the linear stability problem. For the extended model, where we set as an example $\rho = 0.2$, we chose for the additional parameter value

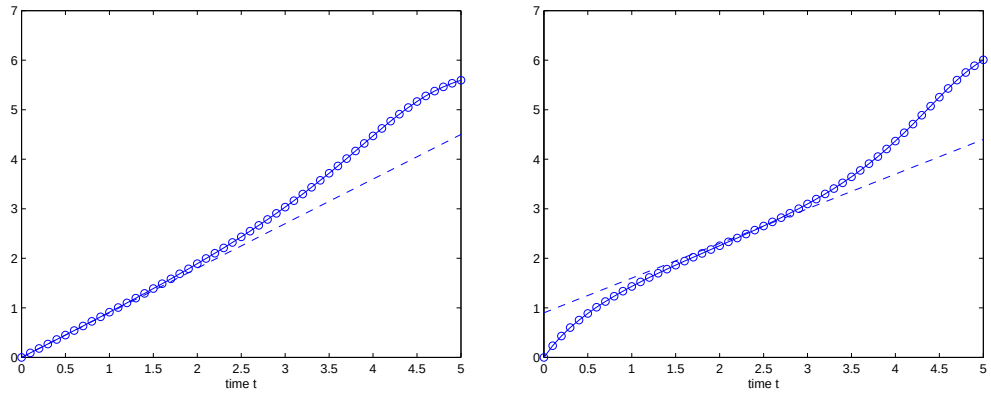

Figure 8: *Comparison of the growth rates for the fully nonlinear and the linearized models:* Left $\rho = 0$*: The dashed line is* $\lambda\, t$*, where* λ *is given by the solution of the linear stability problem, equation (5.5). The curve with the circles denotes* $\ln(||C||)$*.* Right $\rho = 0.2$*: The dashed line shows the long-time behaviour of the solution of equation (5.10). The curve with circles results from the solution to the full problem (3.5).*

$K = 1220$. Here, we observe that the long-time behaviour of the solution of equation (5.10) compares well with the solution to the full problem (3.5). Eventually though, the nonlinear terms begin to have an effect and the solution of the full model deviates from the predictions of the linear model.

6 Comparison of simulations and experiments

6.1 Parameter values

To compare the results from the simulation of our model with those from experiment, it is crucial to have accurate estimates for the parameter values. While the values of most parameters were determined quite accurately from experiment, uncertainties about some of them remained. In table 2 we list the standard set of parameter values.

Here ϵ_2 was determined from experiment (table 1), which yielded the average spatial diffusion coefficient $\epsilon_2 = 0.29\,\mu m^2/s = 0.025$ mm^2/days. Because cells do not change their orientation in a continuous way, ϵ_1 could not be determined from experiment and we let $\epsilon_1 = \epsilon_2$, for simplicity. The values for ρ and K, determined previously in [4], were used as initial guess for a nonlinear least-squares parameter fit to the time evolution of the total mass. The size of the domain L_x, L_y was chosen to match the area observable under the microscope. In [14], the critical angle α was obtained for fibroblast cultures by inspection of relative angles between cells at confluence. Because of the strong similarity between cytokine cultured chondrocytes and fibrob-

lasts, we used the same value here. Since chondrocytes only attach when they are very close to each other, we chose the standard deviation σ for the spatial interaction kernel to be about the length of a single cell. The value of γ essentially sets the convective time scale and was obtained by fitting the cluster size from the simulation to that obtained from experiment – see Section 2.3.

ϵ_1	ϵ_2	γ	α	σ^2	ρ	K	L_x [mm]	L_y [mm]
0.025	0.025	0.0005	20^0	0.01	1.2	40000	3.75	2.75

Table 2: Standard parameter values

6.2 Numerical simulations

Starting from a random initial distribution at $t = 0$, we solve (3.5) using the numerical method described in section 4 and the parameter values listed above. In Fig. 9 snapshots of the cell density at different times are shown. Here at each point $(x, y) \in \Omega$ the marginal spatial cell density of C, that is the integral of $C(x, y, \theta, t)$ over θ, is displayed. The color used at any point (x, y) corresponds to the angle, where $C(x, y, \theta, t)$ is maximal; hence, the color represents the local dominant orientation of the cells. We observe that the number of cells increases uniformly throughout the computational domain Ω, yet past day 6 several patches of cells with a common orientation emerge and settle in a stationary configuration by day 9; note that the total number of cells hardly changes beyond day 6 anymore.

In Fig. 10 we compare the simulation with the experimental data using Gabor filters for post-processing both – see section 2.3. In doing so the spatial resolution of the microscope image was coarsened to match that of the simulation, while the angular dependence over $[0, \pi)$ was divided into four classes, that is sub-intervals of identical lengths, each one assigned with a different color. The cluster size (intersection of $r(s)$ with the x-axis, see Section 2.3) was calculated for three samples from the same donor. By fitting average cluster size from the simulation to that from experiment, between 15 and 20 pixels or about $0.5mm$, we determined the standard value of γ, as shown in Fig. 10.

Once the model has been validated through comparison to experiment, it is instructive to change the value of individual parameters to study their effect on the size and shape of the patterns at confluence. Thus we can also evaluate the parameter sensitivity of the model and address the uncertainties associated with some of the values obtained from experiment. For instance, the reduction of the angular diffusion coefficient ϵ_1 has little effect on the size of the patterns, but the interfaces appear more well-defined in contrast to the standard case: compare Fig. 10 and Fig. 11. An increase in the critical angle α instead, results in larger and increasinlgy irregular patterns, while the uniform spatial population density is maintained, as shown in Fig. 12.

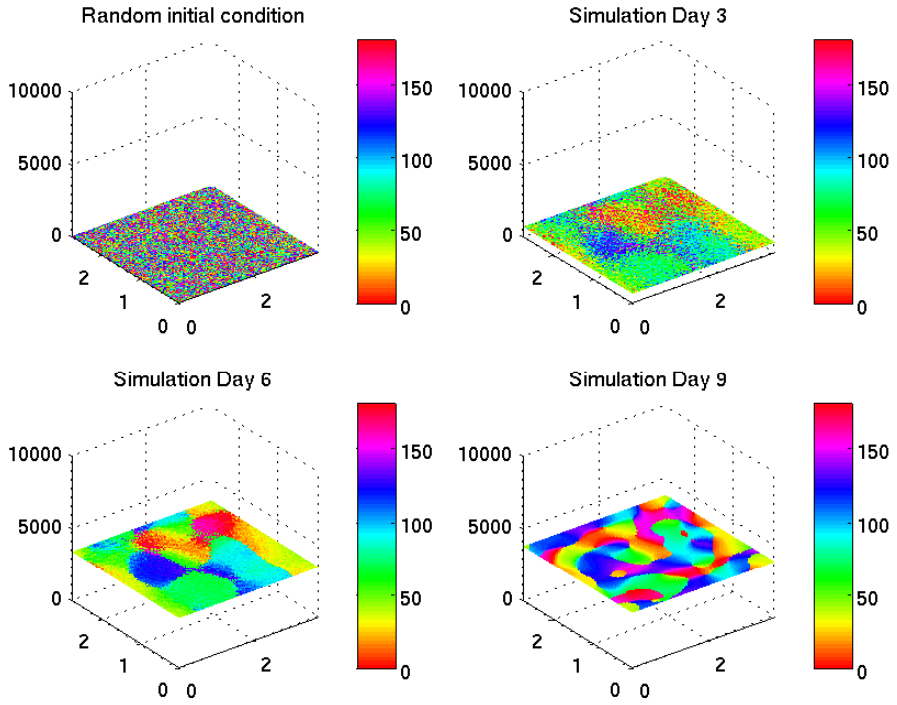

Figure 9: *Snapshots of the cell density at different times. At each point* (x, y) *in the computational domain, the marginal angular density of* C *is shown; the color represents the angle for which* $C(x, y, \theta, t)$ *is maximal.*

7 Concluding remarks

We studied proliferating chondrocyte cells cultured with growth factors such as TFP both experimentally and theoretically. While in a previous work [4] we investigated the impact of these growth factors on quantities such as carrying capacity of the cell culture, the proliferation rate of the cells, here we were interested in the patterns that result at confluence, as their control will be useful in the design of engineered tissue.

To model such a complex growth process of large numbers of interacting cells for long times we chose to revisit the classic models by Mogilner et al. [27] and then extended them to expanding cell populations by incorporating slow logistic growth, with the goal to follow the evolution for long times. This also means that one needs to go beyond linear stability analysis to establish its range of validity. We then established existence of weak solutions of our model rigorously.

An important task of our work was to determine realistic parameters for the resulting logistic integro-differential drift-diffusion type equation. Here we showed how the arising patterns may depend on the various parameter values, which in turn were established from local cell-to-cell interactions and their range, used e.g. to establish

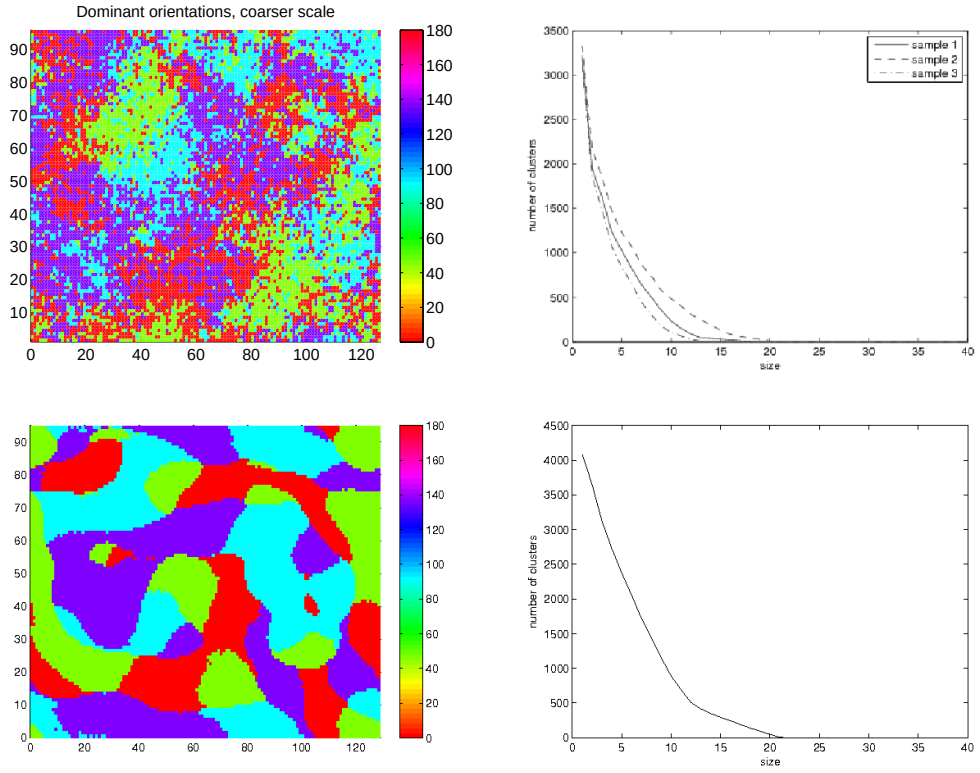

Figure 10: *Comparison of simulation (bottom) with experiment (top). Here color indicates the local dominant orientation of the cells. The cluster size for three samples form the same donor (top) and for the simulation (bottom) are shown on the right.*

critical alignment angles and the scales of the interaction kernels in the model; or the averaged cell motion used to establish diffusion constants. We obtained these values using in part results from our experiments using micro-colony tests, that establish the spatial diffusion coefficient, linear stability analysis to guide us through the range of sets of unstable parameter values. Also, from our previous work, parameters such as carrying capacity and growth rate could be established.

Another task was to set up a numerical code that is robust yielding accurate results for the whole range of parameters as well as the time frame. Here, a variant of the Runge-Kutta method, the Runge-Kutta–Chebyshev method, turned out to be particularly useful to otain a larger stability region than standard methods.

Finally for the actual comparison with the experimentally observed patterns we implemented Gabor filters to visualize the experimental data on orientation, density, and patch sizes. These gave us a good quantitative measure to visualize the patterns.

We performed a number of runs that aimed to show the dependencies of the arising patterns on these parameter values. The parameters which control the formation of the patterns are the scales of the kernels and the ratio between the diffusion and drift coefficients. For example, a small σ leads to the absence of aggregation; we can

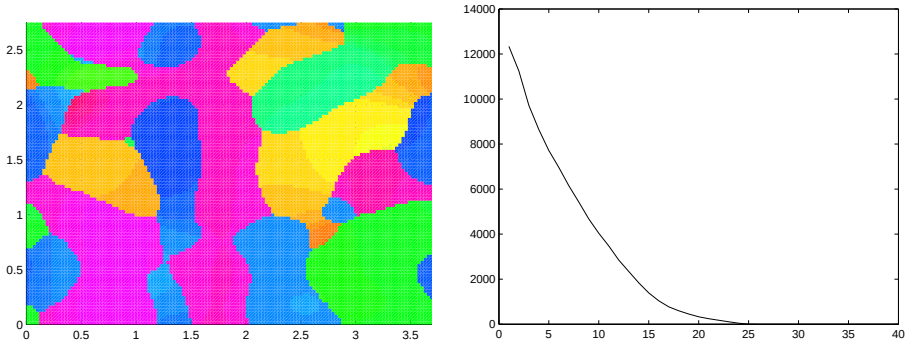

Figure 11: *The cell density is shown at confluence for the standard parameter values in table 2, but with smaller angular diffusion coefficient:* $\epsilon_1 = 0.0025$.

conclude that chondrocytes do not aggregate because they attach only if they are really close, but do not interact in this sense with distant cells. The critical angle α is responsible for the formation of many angular patterns. Letting it be larger leads to a state were only one direction is winning, whereas in our experiments we observed the presence of more arrays, which can be explained by a small critical angle.

Regarding the diffusion and drift coefficients both may contribute to the destabilizationof the solutions. If we fix the diffusion coefficients in the regime of the desired instability, we observe that variations of the drift coefficients lead to different pattern sizes. We observed that doubling γ_1, we double the size of the patterns, meaning that a stronger tendency to align leads to larger patterns. We can obtain similar results changing the angular coefficient: a larger angular velocity, leads to smaller patterns. However, we also observed that the number of winning directions over the whole domain is the same as before, as this quantity is regulated by the critical angle that we took fixed. We can conclude that the total number of winning directions in a culture is regulated by the critical angle, the angle under which the probability that cells align is high, but the distribution of the patterns can be different depending either how high this probability is or how fast the cells change their directions. Guided by these parameter studies we arrived at reasonable parameter values for comparison to the experimentally observed cell patterns at confluence.

While we think that the aproach of using continuum models in combination with some local experimental analysis yields convincing evidence to capture the large scale long-time structure of a proliferating cell culture, our work also leaves a number of open tasks and questions. Apart from the study of aggregation patterns of our model, that has been left open, the determination of the remaining parameters, in particular drift parameters will be an important future task. Through a new set of experimental runs one should also be able to establish more accurately the critical angle for cell alignment for any particular cell culture, without relying on similar cases in the literature.

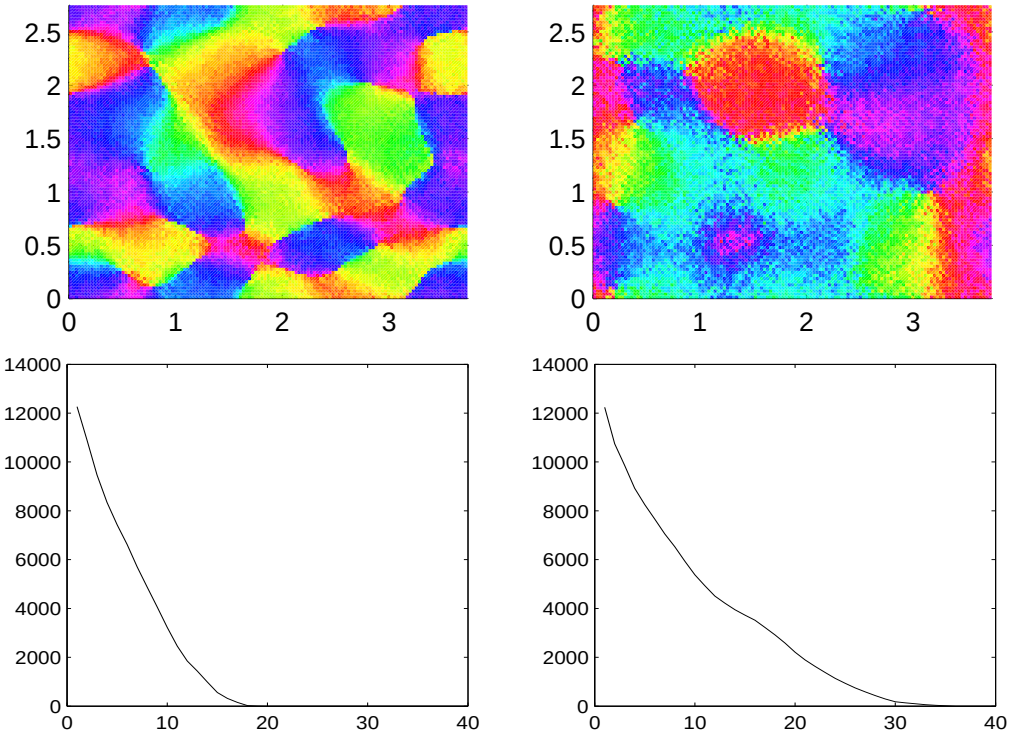

Figure 12: *The cell density is shown at confluence for the standard parameter values in table 2, but with a larger value in the critical angle:* $\alpha = 40^0$ *(left) and* $\alpha = 60^o$ *(right).*

Acknowledgements

We thank Assyr Abdulle, Andreas Münch, Ben Schweizer, Thomas Vetter, Michael Lenziger and Marco Veneroni for useful comments and suggestions.

A Appendix

Proofs of lemmas 3.1, 3.2 and 3.3.

Lemma 3.1:

Proof. Let $C_- = \min(C, 0)$ denote the negative part of C and test equation (3.6) with it. Because the term at the boundary vanish, we have

$$(C', C_-) + (\nabla C, \nabla C_-) = A(C\nabla W * C, \nabla C_-) + (f(C), C_-). \tag{A.1}$$

From a theorem of the function analysis we have that if $C \in H^1_{per}(U)$ then $C_- \in H^1_{per}(U)$; moreover $C' = C'_-$ and $\nabla C_- = \nabla C$ if C is negative. Using this fact, we observe that $(C', C_-) = (C_-{}', C_-)$, $(\nabla C, \nabla C_-) = (\nabla C_-, \nabla C_-)$ and $(f(C), C_-) =$

$(f(C_-), C_-)$; indeed for C positive it is trivial because its negative part is zero and for C negative, $C = C_-$ and the derivatives remain the same.

$$(C_-', C_-) + (\nabla C_-, \nabla C_-) = A(C_- \nabla W * C_-, \nabla C_-) + (f(C_-), C_-) \tag{A.2}$$

Now, using (see [16])

$$(C_-', C_-) = \frac{1}{2}\frac{d}{dt}\int_U |C_-|^2, \tag{A.3}$$

our equation can be reduced to

$$\frac{1}{2}\frac{d}{dt}\int_U |C_-|^2(t) + \int_U |\nabla C_-|^2 = A\int_U C_- \nabla W * C_- \nabla C_- + \int_U f(C_-)C_-. \tag{A.4}$$

Writing down the expression of f, we obtain

$$\frac{1}{2}\frac{d}{dt}\int_U |C_-|^2(t) + \int_U |\nabla C_-|^2 = A\int_U C_- \nabla W * C_- \nabla C_- + \int_U |C_-|^2 - \int_U \int_{-\pi}^{\pi} C_- d\theta |C_-|^2. \tag{A.5}$$

The last term is positive (being C_- negative). Moreover C is bounded, then exist a constant B such that

$$\frac{1}{2}\frac{d}{dt}\int_U |C_-|^2(t) + \int_U |\nabla C_-|^2 \leq A\int_U C_- \nabla W * C_- \nabla C_- + \int_U |C_-|^2 + B\int_U \int_{-\pi}^{\pi} |C_-|^2. \tag{A.6}$$

Since $\nabla W \in L^\infty(U)$ and C is bounded we have $\nabla W * C \in L^\infty(U)$, then $\|\nabla W * C\|_{L^\infty(U)} \leq K$ for a constant $K > 0$. Then, applying the Cauchy inequality

$$\begin{aligned}\int_U C_- \nabla W * C_- \nabla C_- &\leq \|C_-\|_{L^2(U)} \|\nabla W * C_-\|_{L^\infty(U)} \|\nabla C_-\|_{L^2(U)} \leq \\ K\|C_-\|_{L^2(U)} \|\nabla C_-\|_{L^2(U)} &\leq K\left(\frac{1}{4\delta}\|C_-\|^2_{L^2(U)} + \delta\|\nabla C_-\|^2_{L^2(U)}\right).\end{aligned} \tag{A.7}$$

For $\delta = 1/(AK)$ the norm of the gradient vanishes and we finally have

$$\frac{d}{dt}\|C_-\|^2_{L^2(U)} \leq \frac{A^2K^2 + 4 + 4B}{2}\|C_-\|^2_{L^2(U)}. \tag{A.8}$$

From Gronwall's inequality and calling $\eta(t) = \|C_-(t)\|^2_{L^2(U)}$ we obtain

$$\eta(t) \leq e^D \eta(0), \tag{A.9}$$

for $D = \frac{A^2K^2+4+4B}{2}$. But $\eta(0) = 0$ for the choice of the initial conditions. Then is $\eta(t) = 0$, implying that $C_- = 0$ a.e. in U and for all $0 < t < T$, which prove the first part of the theorem. If we now integrate equation (3.6) over the entire domain and applying the Gauss theorem, we obtain

$$\frac{\partial}{\partial t}\int_U C = \int_{\partial U} \nabla C \cdot \vec{n} - A\int_{\partial U} C \nabla W * C \cdot \vec{n} + \int_U f(C), \tag{A.10}$$

where $\vec{n}$ the unit outward normal defined at points of ∂U, normal. For the periodicity of the solution the integrals on the boundary vanish. Since we proved that the function C is positive under our assumptions, we have

$$\frac{\partial}{\partial t}\int_U C = \int_U f(C) = \int_U C - \int_U C \int_{-\pi}^{\pi} C \leq \int_U C. \tag{A.11}$$

We can now apply the Gronwall theorem to the function $\gamma(t) = \int_U C$, to obtain

$$\int_U C \leq e^t \gamma(0) \leq e^T \gamma(0) = e^T \|C(0)\|_{L^1(U)}. \tag{A.12}$$

□

Lemma 3.2:

Proof. By substituting (3.9) in (3.11), we obtain

$$(C_m', w_k) = \left(\left(\sum_{l=1}^m d_m^l(t) w_l\right)', w_k\right) = \sum_{l=1}^m d_m^l{}'(t)(w_l, w_k) = d_m^k{}'(t),$$

for the first term. The other three terms are

$$\begin{aligned}
(\nabla C_m, \nabla w_k) &= \sum_{l=1}^m (\nabla w_l, \nabla w_k) d_m^l(t), \\
(C_m \nabla W * C_m, \nabla w_k) &= \left(\sum_{l=1}^m d_m^l(t) w_l \sum_{l=1}^m d_m^l(t) \nabla W * w_l, \nabla w_k\right), \\
\int_U f(C_m)\, w_k &= \int_U f\left(\sum_{l=1}^m d_m^l(t) w_l\right) w_k.
\end{aligned} \tag{A.13}$$

For fixed k, (3.11) is a first-order system of ordinary differential equations subject to the initial conditions (3.10). Since the right-hand side is Lipschitz-continuous, there exists a unique absolutely continuous function $(d_m^1(t), \ldots, d_m^m(t))$ that satisfies (3.10) and (3.11) for a.e. $0 \leq t \leq T$, at least for small T. Hence C_m defined by (3.9) solves (3.11) for a.e. $0 \leq t \leq T$. □

Lemma 3.3:

Proof. We shall estimate every term on the left side.

1. We multiply (3.11) by $d_k^m(t)$ and sum over k to find

$$(C_m{}', C_m) + (\nabla C_m, \nabla C_m) = A\,(C_m \nabla W * C_m, \nabla C_m) + \int_U f(C_m)\, C_m,$$

for a.e. $0 \leq t \leq T$. From Hölder's inequality we immediately have

$$\frac{d}{dt}\left(\frac{1}{2}\|C_m\|^2_{L^2(U)}\right) + \|\nabla C_m\|^2_{L^2(U)} \leq A\,\|\nabla C_m\|_{L^2(U)}\|C_m\|_{L^2(U)} + \|C_m\|^2_{L^2(U)}.$$

In fact

$$(C_m \nabla W * C_m, \nabla C_m) \leq \|\nabla W * C_m\|_{L^\infty(U)} \int_U C_m \nabla C_m$$

$$\|\nabla W * C_m\|_{L^\infty(U)} = \text{ess}\sup_U |\nabla W * C| = \text{ess}\sup_U \left|\int_U \nabla W(x-x')C(x')dx'\right|$$
$$\leq \text{ess}\sup_U \int_U |\nabla W(x-x')||C(x')| \leq \|\nabla W\|_{L^\infty(U)}\|C_m\|_{L_1(U)} \leq K_1,$$

for our particular choice of W and lemma 3.1. For the boundness of C we havethat $\int_{-\pi}^{\pi} C$ is bounded, then, being C positive, Using the Cauchy inequality, we obtain

$$\frac{d}{dt}\|C_m\|^2_{L^2(U)} + 2\|\nabla C_m\|^2_{L^2(U)} \leq 2AK_1\left(\delta\|\nabla C_m\|^2_{L^2(U)} + \frac{1}{4\delta}\|C_m\|^2_{L^2(U)}\right) + 2\|C_m\|^2.$$

Choosing $\delta = 1/(AK_1)$, $K_2 = (A^2K^2+4)/2$, we have

$$\frac{d}{dt}\|C_m\|^2_{L^2(U)} \leq K_2\|C_m\|^2_{L^2(U)}.$$

If we call $\eta(t) = \|C_m(t)\|^2_{L^2(U)}$, with the Gronwall inequality we obtain

$$\eta(t) \leq e^{K_2 t}\eta(0).$$

Being

$$\eta(0) = \|C_m(0)\|^2_{L^2(U)} \leq \|g\|^2_{L^2(u)},$$

for $K = e^{K_2 T}$, we have the first estimate

$$\max_{0\leq t\leq T}\|C_m(t)\|^2_{L^2(U)} \leq K\|g\|^2_{L^2(U)}.$$

2. Integrating the last equation from 0 to T, we get automatically the second estimate
$$\|C_m(t)\|^2_{L^2(0,T;H^1_{per}(U))} = \int_0^T \|C_m\|^2_{H^1_{per}(U)}dt \leq KT\|g\|^2_{L^2(U)}.$$

3. Fix any $v \in H^1_{per}(U)$, with $\|v\|_{H^1_{per}(U)} \leq 1$, and write $v = v^1 + v^2$, where $v^1 \in$ span$\{w_k\}_{k=1}^m$ and $(v^2, w_k) = 0$, $(k = 1, \ldots, m)$.. Since the functions $\{w_k\}_{k=0}^\infty$ are orthogonal in $H^1_{per}(U)$, $\|v^1\|_{H^1_{per}(U)} \leq \|v\|_{H^1_{per}(U)} \leq 1$. Utilizing 3.11, we deduce for a.e. $0 \leq t \leq T$ that

$$(C_m', v^1) + (\nabla C_m, \nabla v^1) = A\,(C_m \nabla W * C_m, \nabla v^1) + \int_U f(C_m)\,v^1.$$

As $(C'_m, v^1) = (C'_m, v)$ we have

$$(C'_m, v) = -(\nabla C_m, \nabla v^1) + A\,(C_m \nabla W * C_m, \nabla v^1) + \int_U f(C_m)\, v^1.$$

Since $\|v^1\|_{H^1_{per}(U)} \leq 1$ we obtain

$$\begin{aligned} |< C'_m, v >| &\leq \|\nabla C_m\|_{L^2(U)} \|\nabla v^1\|_{L^2(U)} + A\,\|\nabla v^1\|_{L^2(U)} \|C_m\|_{L^2(U)} \\ &+ \|C_m\|_{L^2(U)} \leq K \|C_m\|_{H^1_{per}(U)}. \end{aligned}$$

Therefore

$$\|C'_m\|_{H^{-1}(U)} = |< C'_m, v >|^2 \leq K \|C_m\|^2_{H^1_{per}(U)}.$$

Integrating again between 0 and T

$$\int_0^T \|C'_m\|^2_{H^{-1}(U)} dt \leq K \int_0^T \|C_m\|^2_{H^1_{per}(U)} dt \leq KT \|g\|^2_{L^2(U)}.$$

□

References

[1] Abramowitz M., S.I.A.: Handbook of Mathematical Functions with Formulas, Graphs, and Mathematical Tables. Dover Publications (1964)

[2] A.Gouillou, Lago, B.: Domaine de stabilité associé aux formules d'intégration numérique d'équations différentielles, a pas séparés et a pas liés. recherche de formules a grand rayon de stabilité. Ier Congr. Ass. Fran. Calcul., AFCAL pp. 43–56 (1960)

[3] Barbero, A., Grogan, S., Schafer, D., Heberer, M., Mainil-Varlet, P., Martin, I.: Age related changes in human articular chondrocyte yield, proliferation and post-expansion chondrogenic capacity. Ostearthritis Cartilage **12**, 476–484 (2004)

[4] Barbero, A., Palumberi, V., Wagner, B., Sader, R., Grote, M.J., Martin, I.: Experimental and mathematical study of the influence of growth factors on the growth kinetics of adult human articular chondrocytes. Journal of Cellular Physiology **204**, 830–838 (2005)

[5] Barbero, A., Ploegert, S., Heberer, M., Martin, I.: Plasticity of clonal populations of dedifferentiated adult human articular chondrocytes. Arthritis Rheum **48**, 1315–1325 (2003)

[6] Beattie, G., Cirulli, V., Lopez, A., Hayek, A.: Ex vivo expansion of human pancreatic endocrine cells. J Clin Endocrinol Metab **82**, 1852–1856 (1997)

[7] Carpenter, M., Cui, X., Hu, Z., Jackson, J., Sherman, S., Seiger, A., Wahlberg, L.: In vitro expansion of a multipotent population of human neural progenitor cells. Exp Neurol **158**, 265–278 (1999)

[8] Chipot, M., Edelstein-Keshet., L.: A mathematical theory of size distribution in tissue culture. J. Math. Biol. **16**, 115–130 (1983)

[9] Civelecoglu, G., Edelstein-Keshet, L.: Modelling the dynamics of f-actin in the cell. Bull. Math. Biol. **56**, 587–616 (1994)

[10] Daugman, J.: Uncertainty relations for resolution in space, spatial frequency, and orientation optimized by two-dimensional visual cortical filters. Journal of the Optical Society of America A **2**, 1160–1169 (1985)

[11] Deasy, B., Qu-Peterson, Z., Greenberger, J., Huard, J.: Mechanisms of muscle stem cell expansion with cytokines. Stem Cells **20**, 50–60 (2002)

[12] Deenick, E., Gett, A., Hodgkin, P.: Stochastic model of T dell proliferation: A calculus revealing il-2 regulation of precursor frequencies, cell cycle time, and survival. J. Immunol. **170**, 4963–4972 (2003)

[13] Edelstein-Keshet, L., Ermentrout, G.: Models for contact-mediated pattern formation: cells that form parallel arrays. J. Math. Biol. **29**, 3–58 (1990)

[14] Elsdale, T., Bard, J.: Collagen substrata for studies on cell behaviours. Journal of Cell Biology **54**, 626–637 (1972)

[15] Erickson, C.: Analysis of the formation of parallel arrays in bhk cells in vitro. Exp. Cell Res. **115**, 303–315 (1978)

[16] Evans, L.C.: Partial Differential Equations. American Mathematical Society (1998)

[17] Forsyth, D.A., Ponce, J.: Computer Vision, A Modern Approach. Prentice Hall (2003)

[18] Franklin, J.: Numerical stability in digital and anlogue computation for diffusion problems. J.Math.Phys. **37**, 305–315 (1959)

[19] Gabor, D.: Theory of comminication. J. IEE **93**(26), 429–457 (1946)

[20] Hairer E., W.G.: Solving Ordinary Differential Equation II. Springer-Verlag (2002)

[21] Hairer E. Noersett S.P., W.G.: Solving Ordinary Differential Equations. I: Nonstiff Problems. Springer-Verlag (1987)

[22] Jakob, M., Demarteau, O., Schafer, D., Hinterman, B., Dick, W., Heberer, M., Martin, I.: Specific growth factors during the expansion and redifferentiation of adult human articular chondrocytes enhance chondrogenesis and cartilaginous tissue formation in vitro. J Cell Biochem **81**, 368–377 (2001)

[23] Kress, R.: Linear Integral Equations. Springer-Verlag (1999)

[24] Langer, R., Vacanti, J.: Tissue engineering. Science **260**, 920–926 (1993)

[25] Markoff, C.L.: Ueber polynome, die in einem gegebenen intervall möglichst wenig von null abweichen. Math. Ann. **77**, 213–258 (1916)

[26] Mogilner, A., Edelstein-Keshet, L.: Selecting a common direction, how orientational order can arise from simple contact responses between interacting cells. J. Math. Biol. **33**, 619–660 (1995)

[27] Mogilner, A., Edelstein-Keshet, L.: Spatio-angular order in populations of self-aligning objects: formation of oriented patches. Physica D **89**, 346–367 (1996)

[28] Mogilner, A., Edelstein-Keshet, L., Ermentrout., G.B.: Selecting a common direction. ii. peak-like solutions representing total alignment of cell clusters. J. Math. Biol. **34**, 811–842 (1996)

[29] Sharma, B., Elisseeff, J.H.: Engineering structurally organized cartilage and bone tissues. Annals of biomedical enginnering **32**, 148–159 (2004)

[30] Stewart, J., Masi, T., Cumming, A., Molnar, G., Wentworth, B., Sampath, K., McPherson, J., Yaeger, P.: Characterization of proliferating human skeletal muscle-derived cells in vitro: differential modulation of myoblast markers by tgf-beta2. J Cell Physiol **196**, 70–78 (2003)

[31] Trefethen, L., Trefethen, A., Reddy, S., Driscoll, D.: Hydrodynamics without eigenvalues. Science **261**, 578 (1993)

[32] Trinkaus, J.P.: Further thoughts on directional cell-movement during morphogenesis. Journal of Neuroscience research **13**, 1–19 (1985)

[33] Yuan, C.: Some difference schemes for the solution of the first boundary value problem for linear differential equations with partial derivatives. Master's thesis, Moscow State University (1958)